Computers & Geosciences 156 (2021) 104880

Contents lists available at ScienceDirect

Computers and Geosciences

journal homepage: www.elsevier.com/locate/cageo

Research paper

Plunging criterion for particle-laden flows over sloping bottoms: Three-dimensional turbulence-resolving simulations

Felipe N. Schuch [a,b,*], Eckart Meiburg [b], Jorge H. Silvestrini [a]

[a] School of Technology, Pontifical Catholic University of Rio Grande do Sul, Porto Alegre, Brazil
[b] Department of Mechanical Engineering, University of California Santa Barbara, Santa Barbara, CA 93106, USA

ARTICLE INFO

Dataset link: https://doi.org/10.5281/zenodo.4044388

Keywords:
Plunging flow
Plunging criterion
Turbidity current
Large-eddy Simulation

ABSTRACT

Hyperpycnal flows are observed when the density of a fluid entering into a quiescent environment is greater than that of the ambient fluid. This difference can be due to salinity, temperature, concentration, turbidity, or a combination of them. Over a sloping bottom, the inflowing momentum decreases progressively until a critical stage is reached where the inflow plunges underneath the ambient and flows adjacent to the bed as an underflow density current. In the present work, a new equation is proposed in order to predict the critical depth for plunging, i.e., the plunging criterion. It differs from previous studies since it includes the role of the settling velocity and the bed slope. The high spatiotemporal resolution from twelve original numerical simulations allows us to validate the initial hypotheses established, in addition to numerical and experimental data available in the literature, and good agreement is found between them. A negative value for the mixing coefficient was observed for the first time for the hyperpycnal flow in a tilted channel. This indicates that if the settling velocity of the suspended material is high enough, the submerged flow may lose fluid to the environment (detrainment), instead of incorporating it. The proposed plunging criterion may assist in the design of future experimental or numerical works.

1. Introduction

A turbidity current entering a lighter ambient fluid is classified as hyperpycnal, so that it is expected to propagate near the bed, below the ambient fluid, due to buoyancy forces. Such flows are an important instrument for the transport of fluvial, littoral and shelf sediments into deeper waters (Garcia, 1994), causing deposition, erosion and even material resuspension from the sea floor. Old sand deposits formed by turbidity currents can preserve important climatic and tectonic evidence, they can record river flood dynamics and, under the right conditions, become hydrocarbon reservoirs (Mulder et al., 2003; Lamb and Mohrig, 2009; Meiburg and Kneller, 2010). Turbidity currents and their deposits are also observed in dam reservoirs, being responsible for reducing the capacity and affecting structures such as powerhouse intakes and bottom outlets (Chamoun et al., 2016). Additionally, turbidity currents are a potential hazard to submarine telecommunication cables, well heads, and oil and gas pipelines (Meiburg et al., 2015; Sequeiros et al., 2019; Porcile et al., 2020) , furthermore, such flows can strongly affect marine ecosystems near river mouths (Horner-Devine et al., 2015).

In the case of an influx at the highest edge of an sloping bottom, the flow momentum can be sufficient to push the lighter fluid downstream. However, the flow velocity decreases while the depth increases in the streamwise direction, due to the bed slope. In this way, at sufficient depth, buoyancy forces overcome the inertial forces, the flow collapses and plunges. This phenomenon is noticed in natural environments such as ocean, lakes and dam reservoirs. A schematic representation is shown in Fig. 1, where the three main regions of the plunging of the hyperpycnal flow are visible. The influx is characterized by its initial depth $\tilde{h}_0$ ($\tilde{\cdot}$ corresponds to dimensional quantities), volumetric discharge per unit width $\tilde{Q}_0$, and a fresh water density plus an excess due to suspended material $\tilde{\rho}_w + \Delta\tilde{\rho}$ entering an ambient with different density $\tilde{\rho}_a$. Ideally, the depth-limited plume is a homogeneous flow region that occupies the complete channel depth, dominated by inertial forces. It is a valid assumption for this work, however, some density stratification may be observed in natural settings and the velocity profile may not be homogeneous, since they depend on the boundary conditions. At sufficient depth $\tilde{H}_p$, the flow collapses, in the so-called plunge region. Downstream, the flow assumes the form of a turbidity current, dominated by buoyancy forces, and new values of depth $\tilde{H}_d$, discharge $\tilde{Q}_d$ and density $\tilde{\rho}_a + \Delta\tilde{\rho}_d$ are observed due to the continuous mixing between ambient fluid and the underflow, which is expressed

* Corresponding author at: School of Technology, Pontifical Catholic University of Rio Grande do Sul, Porto Alegre, Brazil.
E-mail addresses: felipe.schuch@edu.pucrs.br (F.N. Schuch), meiburg@engineering.ucsb.edu (E. Meiburg), jorgehs@pucrs.br (J.H. Silvestrini).

https://doi.org/10.1016/j.cageo.2021.104880
Received 21 October 2020; Received in revised form 15 June 2021; Accepted 2 July 2021
Available online 6 July 2021

Nomenclature

Notation

Δt	Time step
γ	Mixing coefficient
ν	Kinematic viscosity
ρ	Density
ξ	$r_0 u_s / S$
C	Layer-averaged concentration
c	Scalar concentration
d_s	Grain size
Fr	Densimetric Froude number
Fr_0^*	Maximum initial Froude number for plunging
g	Gravitational acceleration
g'	Reduced gravity
H	Underflow depth
h	Channel depth
H_p^*	Maximum flow depth possible
L_i	Domain size in direction i
L_{1b}	Sponge zone length
L_{2b}	Height of immersed boundary method layer
n_i	Number of mesh nodes in direction i
p	Pressure
Q	Layer-averaged flow rate
R	Sediment reduced density
r_0	Shape factor for vertical concentration profile
Re	Reynolds number
S	Bed slope
Sc	Schmidt number
t	Time
U	Layer-averaged velocity
u_i	Velocity vector
u_s	Settling velocity
x_i	Coordinate system

Subscripts

0	Initial value, at inflow
a	Ambient flow
d	Downstream plunging
f	At front position
p	At plunge position
s	Sediment
w	Fresh water

by the mixing coefficient

$$\gamma = \tilde{Q}_d / \tilde{Q}_0 - 1. \tag{1}$$

An ambient counterflow is induced in the opposite direction. This balance between inertial and buoyancy forces is a key point in the study of the plunging flow, it can be represented by the initial densimetric Froude number

$$Fr_0 = \frac{\tilde{Q}_0}{\sqrt{R\tilde{C}_0 \tilde{g} \tilde{h}_0^3}}, \tag{2}$$

where $R = (\tilde{\rho}_s - \tilde{\rho}_w)/\tilde{\rho}_w$ is the submerged specific density of sediments, $\tilde{\rho}_s$ is the density of the sediment, $\tilde{C}_0$ is the volumetric concentration of sediments at the inlet and $\tilde{g}$ is the gravitational acceleration.

There are two necessary conditions for the plunge to happen. First, the inflowing turbidity current must be denser than the ambient fluid, the necessary suspended particle concentration to overcome the ambient density can be written as

$$\tilde{C}_c = \frac{1}{R}\left(\frac{\tilde{\rho}_a}{\tilde{\rho}_w} - 1\right), \tag{3}$$

according to Lamb et al. (2010). The equation makes evident that in the case of freshwater ambient ($\tilde{\rho}_a = \tilde{\rho}_w$), any concentration is enough to satisfy the first condition. Second, the channel needs to be deep enough for the turbidity current to collapse. The critical depth for plunging $\tilde{H}_p$, also called plunging criterion, can be derived from (2) and written as a function of a constant K (often computed empirically from numerical and/or experimental data), initial flow rate $\tilde{Q}_0$ and reduced gravity acceleration $\tilde{g}' = R\tilde{C}_0\tilde{g}$ (Singh and Shah, 1971; Akiyama and Stefan, 1984), as follow

$$\tilde{H}_p = K\left(\frac{\tilde{Q}_0^2}{\tilde{g}'}\right)^{\frac{1}{3}}, \tag{4}$$

or it can be expressed in dimensionless form as

$$\frac{\tilde{H}_p}{\tilde{h}_0} = H_p = \left(\frac{Fr_0}{Fr_p}\right)^{\frac{2}{3}}, \tag{5}$$

where Fr_0 and Fr_p are the initial densimetric Froude number and the densimetric Froude number at the plunge location, respectively, and $\tilde{h}_0$ is the initial channel depth. Notice that both notations are equivalent ($Fr_p \approx K^{-3/2}$). Many experiments and numerical simulations have been performed in the interest of investigate K (or Fr_p) and how it is affected by the flow parameters.

Singh and Shah (1971) investigated the plunging criterion by performing a two-dimensional experimental study. The obtained depth for plunging was compared with the initial flow discharge and reduced gravity (4), and the results suggest that $K = 1.3$, which leads to $Fr_p = 0.67$. Farrell and Stefan (1986) used temperature in order to control the density difference necessary for plunging, their methodology includes physical experiments in addition to 2D-RANS numerical simulations, based on the standard $k-\epsilon$ model. The authors reported a mixing coefficient of $\gamma = 0.1$, and the plunging criterion $K = 1.3$ for their experiments, confirming the previous results from Singh and Shah (1971), and $K = 1.6$ ($Fr_p = 0.49$) for the numerical simulations. Several experiments were conducted by Lee and Yu (1997), including conservative (saline) and not conservative (Kaolin in suspension) currents. The study included the migration of the plunge point, in what they called the incipient plunge location. For the stable plunge position, $Fr_p = 0.6$ was reported. The authors found that the effective density difference at the plunge point characterizes the event, and it does not depend on the presence of the suspended particles (Kaolin) or lack of it (saline cases). Kassem and Imran (2001) conducted a set of 2D-RANS simulations. Their numerical model was employed to reproduce both laboratory, based on the experiments of Singh and Shah (1971), and field scales, using the data available in Mulder et al. (1998). Dai et al. (2007), different from previous works, presented nine different cases using 2D-LES, based on the Smagorinsky model. They reported that $K = 1.8$, which can be rearranged to $Fr_p = 0.41$, besides an initial mixing coefficient of $\gamma_0 = 15\%$. Arita and Nakai (2008) presented two-dimensional laboratory experiments for the plunging of a saline current. According to these authors, the flow under investigation can be categorized into one of four groups, according to the initial densimetric Froude number Fr_0 and bed slope S. For the Type III, that is comparable with our numerical study, they found that $Fr_p \approx 0.5$. Lamb et al. (2010) shows an experimental study of turbidity currents, presenting seven experiments with different values for initial flow discharge $\tilde{Q}_0$ and initial volumetric concentration $\tilde{C}_0$ of crushed silica. The results show that $Fr_p \approx 0.45$ is a reasonable value, together with the initial mixing coefficient $\gamma = 0.2$, and good agreement was found with the analytical model of Parker and Toniolo (2007). Besides, they concluded that the required fluvial sediment concentration to create a plunging

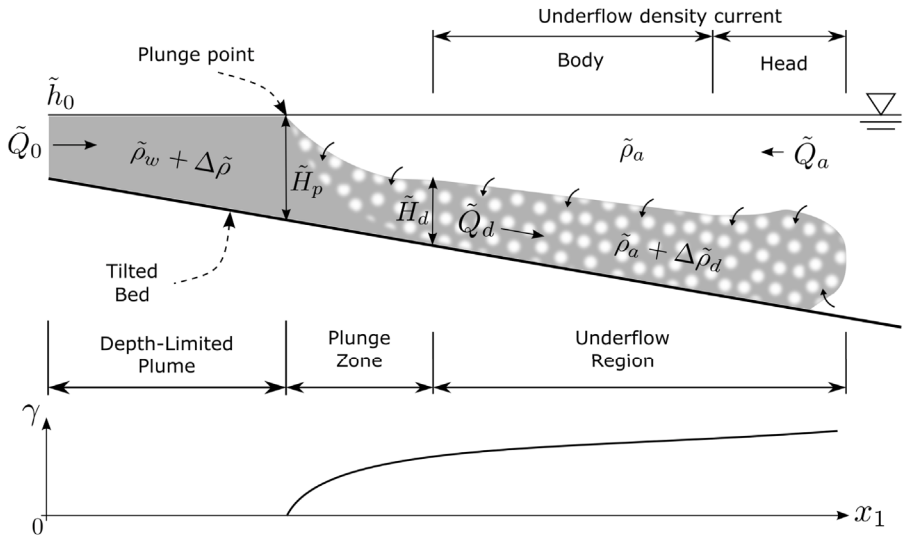

Fig. 1. Representation of a hyperpycnal flow over sloping bottom. The mixing coefficient γ according to Eq. (1) is presented for reference.
Source: Modified from Schuch et al. (2018).

flow can be significantly higher than the concentration conventionally used assuming density similarity by virtue of the deposition upstream of the plunge point. Schuch et al. (2018) presented four three-dimensional turbulence-resolved simulations (3D-LES) and the results were compared with the experiments of Lamb et al. (2010) and the analytical model of Parker and Toniolo (2007) in order to validate the new numerical framework proposed by the author, and good agreement was found between them, $Fr_p \approx 0.45$ was recovered. Schuch et al. (2020) examine a different aspect of the previous numerical study (Schuch et al., 2018) and reported $Fr_p = 0.43$. Besides that, the authors presented an original data-set that registers the entire Spatio-temporal evolution of the plunge phenomenon and all relevant quantities.

There are theoretical works about the plunging flow as well, based on integral equations, conservation laws and box model analysis. Akiyama and Stefan (1984) presented a review of all previous theoretical works. They proposed a prediction of the depth at the plunge point with regards to the core parameters that describe the event, including the bed slope S, initial densimetric Froude number Fr_0, total friction coefficient f_t and the initial mixing coefficient γ_0. Their prediction agrees well with laboratory and field data. However, according to their study plunging is not possible without mixing ($\gamma = 0$). Parker and Toniolo (2007) and Dai and García (2009) proposed a correction in the previous analysis of Akiyama and Stefan (1984) and discussed that plunging is possible without mixing, such as in a water/oil configuration. According to the authors, the densimetric Froude number at the plunge position Fr_p and downstream plunging Fr_d, besides the ratio between flow depth at the plunge point $\tilde{H}_p$ and downstream plunging $\tilde{H}_d$ can be expressed as function of the mixing coefficient γ only. Notice that there is no way to know γ_0 a priori, which is found by using numerical simulations.

The primary purpose of the current work is to present a novel methodology for the prediction of the critical depth required for plunging (or plunging criterion). Unlike previous models, the role played by the settling velocity of the suspended material is included, since the sedimentation occurring in the depth-limited zone (see Fig. 1) could reduce the effective concentration in the plunging zone in an order of magnitude in comparison with that at the inlet condition, following the findings of Lee and Yu (1997) and Lamb et al. (2010) described above. In addition, twelve numerical simulations are presented in order to validate the proposed model, considering four different bed slopes and three different settling velocities. The manuscript is organized in seven sections: an introduction, a description of the governing equations, computational setup, the numerical methodology for the simulations, a description of the proposed equation for the prediction of the plunging depth, a results section presenting the numerical data and the validation of the new model, and a conclusion.

2. Governing equations

For the current work, the transport equation under the Boussinesq approximation can be employed for turbidity currents or for conservative currents (when settling velocity is equal to zero), in addition to the incompressible Navier–Stokes equations. They are formulated in the dimensionless context as

$$\frac{\partial u_j}{\partial x_j} = 0, \tag{6a}$$

$$\frac{\partial u_i}{\partial t} = -u_j \frac{\partial u_i}{\partial x_j} - \frac{\partial p}{\partial x_i} + \frac{1}{Re}\frac{\partial^2 u_i}{\partial x_j \partial x_j} + e_i^g \frac{c}{Fr_0^2}, \tag{6b}$$

$$\frac{\partial c}{\partial t} = -\left(u_j + u_s e_j^g\right)\frac{\partial c}{\partial x_j} + \frac{1}{ReSc}\frac{\partial^2 c}{\partial x_j \partial x_j}, \tag{6c}$$

where c, p and u_i represent the scalar concentration, pressure and the flow velocity, respectively, along with the coordinate system x_i, time t and the unit vector pointing in the direction of gravity $e^g = [0, 1, 0]$ (see Fig. 2). The settling velocity u_s is associated to the grain size by the Stokes settling velocity law (Julien, 2010) which assumes that the foremost flow force acting on an isolated particle is the Stokes drag. The initial densimetric Froude number is defined in Eq. (2). The Reynolds and Schmidt numbers, and the Stokes settling velocity are specified as

$$Re = \frac{\tilde{Q}_0}{\tilde{\nu}}, \tag{7a}$$

$$Sc = \frac{\tilde{\nu}}{\tilde{D}}, \tag{7b}$$

$$u_s = \frac{\tilde{u}_s \tilde{h}_0}{\tilde{Q}_0} = \frac{\tilde{d}_s^2 R \tilde{g} \tilde{h}_0}{18 \tilde{\nu} \tilde{Q}_0}, \tag{7c}$$

where $\tilde{Q}_0$ is the volumetric discharge per unit width, defined as the product of the inlet velocity $\tilde{U}_0$ and the initial depth $\tilde{h}_0$. The kinematic viscosity is $\tilde{\nu}$, the diffusivity of particle concentration is $\tilde{D}$ and the characteristic grain size is denoted as $\tilde{d}_s$. All variables and parameters are made dimensionless using the influx depth $\tilde{h}_0$, velocity $\tilde{U}_0$ and sediment concentration $\tilde{C}_0$.

3. Computational setup

The computational setup, as presented in Fig. 2, is derived from the previous study of Schuch et al. (2018), however, a few improvements

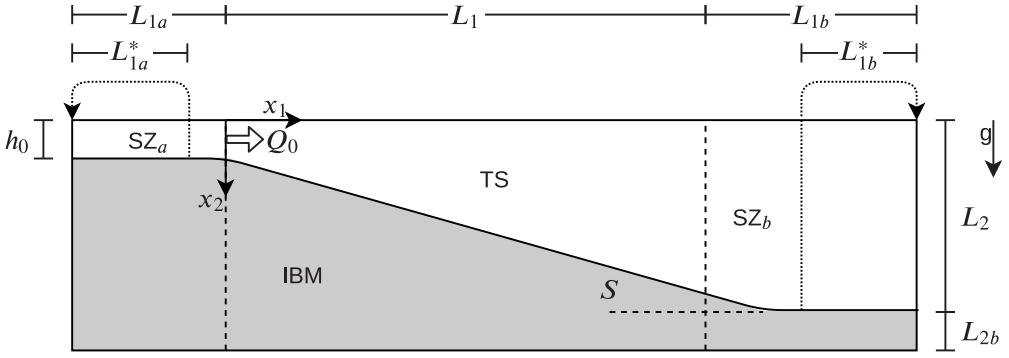

Fig. 2. Graphic representation of the computational setup (not to scale). Spanwise coordinate x_3 is perpendicular to the plane. It is divided in four sections: In gray, the tilted bed is inserted by Immersed Boundary Method (IBM); TS represents the test section; SZ_a represents the Sponge Zone upstream of TS; SZ_b represents the Sponge Zone downstream of TS.

are proposed. The test section (TS) is the region where the flow is analyzed. The bed slope S is included in the computational domain via a customized immersed boundary method (IBM) (Gautier et al., 2014).

Two sponge zones are employed to mimic in the computational domain the key aspects of the inlet (head box) and outlet (vent drain) of experimental tanks. Firstly, SZ_a is located upstream of the test section and provides the particle-laden flow. Besides that, a recycling technique $u_i(-L_{1a}, x_2, x_3) = u_i(-L_{1a} + L^*_{1a}, x_2, x_3)$ is used in order to ensure a turbulent inflow condition. Secondly, SZ_b applies near the outflow boundary an intrinsic vertical profile for the streamwise velocity $u_1(x_i)$, in order to reduce the turbulence level to zero. This vertical profile is obtained by means of a spanwise average and a moving average in time in a reference position, upstream of the outflow boundary. As suggested by Henniger et al. (2010), the numerical domain should be long enough to promote the deposition of the entire suspended material, however, this approach is very computationally demanding. Following Schuch et al. (2018), an absorption coefficient is defined in order to remove suspended concentration upstream of the outlet, significantly decreasing computational costs. Note SZ_a and SZ_b are operative only upstream and downstream of the test section, respectively, so that the flow and statistics in the test section are not affected.

A nondeformable water surface is assumed for the top boundary condition (where $x_2 = 0$), which is described for a no-flux condition for the particle concentration and a free-slip condition for the velocity field, following Nasr-Azadani et al. (2013). At the solid–fluid interface x_{2f} (bed position), a no-slip condition is used for the carrier fluid and a convective outflow condition in the vertical direction x_2 reproduces the particle deposition (Necker et al., 2002). Notice this framework allows deposition, but ignores erosion and does not change the bed topography. Regular 1-D convection equations are employed at the outflow boundary ($x_1 = L_1 + L_{1b}$) for the scalar and for the velocity. Periodic boundary conditions are assumed for concentration and velocity for the spanwise direction x_3. In a preliminary study, the use of periodic or free-slip conditions in the spanwise direction has not shown any significant difference regarding the quantities measured and presented in this work. For the initial condition (when $t = 0$) the domain is defined as fresh-water ($c = 0$) at rest ($u_i = 0$).

For the complete mathematical description of the computational setup, including sponge zones, boundary conditions, and initial conditions, we refer the reader to the code repository (see Computer Code Availability).

4. Numerical methodology

The numerical simulations were carried out by `Xcompact3d` (Bartholomew et al., 2020), an open source tool based on a Boussinesq system for incompressible fluids, designed for supercomputers (see computer code availability). The code is based on high-order finite-difference schemes and a predictor–corrector method for the Navier–Stokes equations, which leads to the solution of a Poisson equation for the pressure. With a spectral approach using three-dimensional Fast Fourier transforms (FFTs) and the view of modified wavenumbers (Lele, 1992) for this equation, the divergence-free condition is ensured up to machine accuracy. In order to prevent spurious pressure oscillations, the pressure mesh is staggered from the other variables by half a mesh. More information regarding the numerical aspects of `Xcompact3d` are available in Laizet and Lamballais (2009). The computational domain is divided into several pencils, each one solved by a different MPI-process, resulting on a highly scalable 2D domain decomposition. A complete description concerning the parallel strategy can be found at Laizet and Li (2011).

The governing Eqs. (6) are solved by an implicit Large-Eddy Simulations approach, in with only the largest and energy-containing flow structures are resolved. On the other hand, the small scales are not resolved, instead, they are modeled via artificial dissipation that acts when computing the viscous term (Sagaut, 2006; Grinstein et al., 2007). Lamballais et al. (2011) and Dairay et al. (2017) presented a new set of coefficients for the sixth-order compact finite-difference schemes, configured to be over-dissipative at the highest wave numbers and to control the aliasing errors via the viscous term. Notice that the solution differs from the classic high-order finite-difference scheme only at highest wave numbers, where even the latter becomes less accurate.

For the validation of the numerical framework presented here for the problem demonstrated in Fig. 1 we refer the reader to the complete comparison between numerical, experimental and analytical models provided in Schuch et al. (2018).

5. Plunging condition

The role that each parameter plays with regard to the necessary depth required for plunging is well known. Keeping everything else constant, the plunge position moves downstream due to:

- An increase in the initial densimetric Froude number Fr_0, as this means increasing the ratio of inertial forces to the buoyant forces at the channel entrance, so that a greater depth for plunging is expected;
- An increase in the settling velocity u_s of the suspended sediments, as their sedimentation in the depth-limited zone (see Fig. 1) reduces the effective concentration in the plunge zone, and again a greater depth for plunging is expected; Notice this is valid only in a moderate range of u_s, since other processes may occur if the flow does not have the ability to keep coarse material in suspension.
- Finally, by reducing the bed slope S, as the current would have to travel a greater distance to reach the same critical depth and plunge.

The above parameters can be combined in order to provide an estimate of the plunging condition, based on the streamwise x_1 evolution of the densimetric Froude number, that can be computed as

$$Fr(x_1) = \frac{\tilde{Q}(x_1)}{\sqrt{R\tilde{C}(x_1)\tilde{g}\tilde{H}^3(x_1)}}, \tag{8}$$

or the right-hand side can be written in a dimensionless form, as a function of the inlet Froude Number and other parameters, the resulting equation is

$$Fr(x_1) = \frac{Q(x_1)}{\sqrt{C(x_1)H^3(x_1)}} Fr_0. \tag{9}$$

All values are considered in a layer-averaged context per unit width, computed following Ellison and Turner (1959) according to the equations

$$Uh(x_1) = \frac{1}{L_3}\int_0^{L_3}\int_{x_{2r}}^{x_{2i}} u_1(x_i)dx_2dx_3, \tag{10a}$$

$$U^2h(x_1) = \frac{1}{L_3}\int_0^{L_3}\int_{x_{2r}}^{x_{2i}} u_1^2(x_i)dx_2dx_3, \tag{10b}$$

$$UCh(x_1) = \frac{1}{L_3}\int_0^{L_3}\int_{x_{2r}}^{x_{2i}} u_1(x_i)c(x_i)dx_2dx_3. \tag{10c}$$

For the vertical integration, x_{2i} represents the interface between the underflow density current and the ambient fluid (see Fig. 1), considered in this work as the position where $u_1 c = 0.025$. The position where $u_1 = 0$ is often considered as the interface; however, two problems have been identified when using it. First, it is not appropriate during the initial phase because the incipient plunge zone moves downstream from the inlet boundary with a velocity greater than zero (see Fig. 4). Second, it is not convenient for the cases were the ambient fluid moves in the same direction as the underflow (see Fig. 7c). Including the concentration in the criterion to locate the interface solves both issues. Finally, the layer-averaged velocity U, flow depth H, flow discharge Q and concentration C are computed respectively as

$$U(x_1) = U^2h/Uh, \tag{11a}$$

$$H(x_1) = (Uh)^2/U^2h, \tag{11b}$$

$$Q(x_1) = Uh, \tag{11c}$$

$$C(x_1) = UCh/Uh. \tag{11d}$$

In order to link the Froude number at the plunge position Fr_p with the Froude number at the inlet Fr_0, three assumptions are established: first, the flow rate at the depth-limited zone (see Fig. 1) is constant, and by definition the dimensionless value is equal to unity; second, the layer-averaged concentration decays exponentially with x_1 due to sedimentation (Lamb et al., 2010), downstream of the entrance at the test section. It is expressed as a function of the settling velocity u_s and a shape factor r_0 (the ratio between near bed concentration and layer-averaged concentration (Parker et al., 1987)); third, distance for plunging x_p is known using geometry. They are written as

$$Q_0 = Q_p = 1, \tag{12a}$$

$$C_p = \exp(-u_s r_0 x_p), \tag{12b}$$

$$x_p = \frac{H_p - 1}{S}. \tag{12c}$$

The equation for the plunging criterion is obtained by applying (12) into (9), resulting in

$$\left(\frac{Fr_0}{Fr_p}\right)^{\frac{2}{3}} = H_p \exp\left(-\xi\frac{H_p - 1}{3}\right), \tag{13}$$

where $\xi = r_0 u_s/S$. In this way, the depth for plunging H_p can be evaluated numerically (Fig. 3) as function of three characteristic parameters (u_s, S and Fr_0), besides two constants that should be estimated (Fr_p and r_0). Notice that if $u_s = 0$, Eq. (13) is identical to Eq. (5).

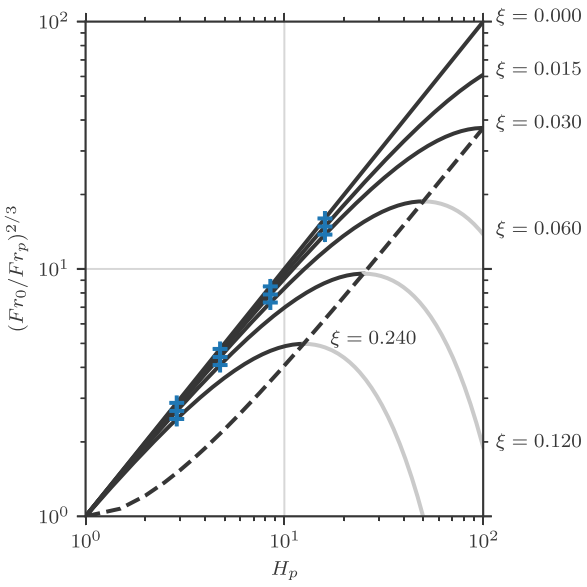

Fig. 3. Depth for plunging H_p computed according to (13), solid lines indicate different values for $\xi = r_0 u_s/S$. The dashed line indicates the limits according to (14), the lines are presented in gray beyond the limits, for reference. The plus marks indicate the twelve proposed simulations..

Analyzing Eq. (9), there is a compensation process for the densimetric Froude number while the plunge point moves downstream of the inflow. Due to the tilted bed, the flow depth increases with x_1 and lowers the local Froude number, while sedimentation reduces the depth-averaged concentration with x_1 and thereby increases the local Froude number. As a result, depending on the ratio between settling velocity and bed slope, or simply ξ, the flow may become homopycnal and never reach the critical local Froude number to plunge if its initial value Fr_0 is above a certain threshold Fr_0^*. It is possible to obtain this key value from (13). First, the theoretical maximum flow depth possible H_p^* for a given value of ξ can be found at the maximum value at the right-hand side of (13). Then, by substituting it back in the equation, the maximum initial Froude number Fr_0^* for plunging is obtained. They are written as

$$H_p^* = \frac{3}{\xi}, \tag{14a}$$

$$\left(\frac{Fr_0^*}{Fr_p}\right)^{\frac{2}{3}} = \frac{3}{\xi}\exp\left(\frac{\xi}{3} - 1\right), \tag{14b}$$

where no plunging is expected if $Fr_0^* < Fr_0$. These limits are presented as the dashed line in Fig. 3, for reference.

6. Results

Twelve simulations are conducted, aiming to validate the predicted plunge depth given by Eq. (13). Bed slopes S of 1.25%, 2.5%, 5% and 10%, besides settling velocities u_s of 0, 0.0015 and 0.003 are employed. In order to have a appropriate comparison between the different cases, the expected distance for plunging x_p is set to $150h_0$, however, the depth is not the same, since it is a function of the bed slope S (12c). The initial densimetric Froude number for each case is computed according to Eq. (13), setting $r_0 = 1$ and $Fr_p = 0.45$. The parameters are shown at Table 1, while Reynolds number Re is equal to 2500 and Schmidt number Sc is equal to one for all simulations. Note the value of Fr_0 is unique for each of the simulations, so it is impossible to analyze the rule of a parameter individually.

All the parameters and results presented in this section are dimensionless. However, the experimental configuration of Lamb et al.

Table 1
Summary of the different simulation conditions: bed slope S, settling velocity u_s and initial densimetric Froude number Fr_0. In addition, the main results: distance for plunging x_p, flow depth, concentration, and densimetric Froude number at the plunge point (H_p, C_p and Fr_p, respectively) and downstream, where $x_1 = 250h_0$ (H_d, C_d and Fr_d, respectively), and the mixing coefficient γ_d. Notice the dimensionless values for initial depth h_0, discharge Q_0 and concentration C_0 are equal to unity by definition.

Run	S%	$u_s \times 10^2$	Fr_0	x_p	H_p	C_p	Fr_p	H_d	C_d	Fr_d	γ_d
1.25–0	1.25	0.00	2.19	150.62	2.74	0.99	0.49	1.60	0.78	1.51	0.22
1.25–15	1.25	0.15	1.96	169.69	2.85	0.74	0.47	1.43	0.56	1.68	0.09
1.25–30	1.25	0.30	1.75	130.62	2.48	0.61	0.58	1.14	0.33	2.27	−0.10
2.5–0	2.50	0.00	4.66	149.38	4.52	1.00	0.48	2.47	0.77	1.70	0.23
2.5–15	2.50	0.15	4.16	171.56	4.89	0.72	0.45	2.09	0.57	1.94	0.04
2.5–30	2.50	0.30	3.72	148.12	4.49	0.56	0.51	1.55	0.36	2.60	−0.20
5.0–0	5.00	0.00	11.15	149.69	7.63	1.00	0.53	4.62	0.73	1.70	0.28
5.0–15	5.00	0.15	9.97	158.44	7.50	0.74	0.57	3.80	0.52	2.05	0.08
5.0–30	5.00	0.30	8.90	151.56	7.47	0.60	0.53	2.24	0.39	3.15	−0.27
10.0–0	10.00	0.00	28.80	179.38	13.61	0.99	0.58	8.71	0.68	1.77	0.29
10.0–15	10.00	0.15	25.74	187.81	16.56	0.70	0.45	6.42	0.54	2.18	−0.00
10.0–30	10.00	0.30	23.00	177.19	14.95	0.56	0.47	4.15	0.39	3.02	−0.32

Table 2
Domain height $L_2 + L_{2b}$ and mesh nodes in the vertical direction n_2 as function of bed slope S.

S%	1.25	2.5	5	10
$L_2 + L_{2b}$	$6.75h_0$	$10.125h_0$	$16.875h_0$	$33.75h_0$
n_2	49	73	121	241

(2010) can be used to express the values in the dimensional space, as a reference. The initial depth $\tilde{h}_0$ and the sediment reduced density R were reported by the authors as 10 mm and 1.65, respectively. With this data, the volumetric flow discharge per width unit at the inlet $\tilde{Q}_0$ can be computed as 0.0025 m^2/s(7a), for all simulations. According to Eq. (7c), the equivalent grain sizes $\tilde{d}_s$ would be 21 μm and 29 μm for the setting velocities 0.0015 and 0.0030, respectively. The volumetric particle concentration at the inlet $\tilde{C}_0$ ranges from 0.04% to 12%, the exact value for each case can be obtained using Eq. (2).

The numerical configuration of the presented simulations is based on the experimental channel setup of Lamb et al. (2010) and the numerical study of Schuch et al. (2018). The test section dimensions are $(L_1, L_3) = (250.0h_0, 8.0h_0)$. The horizontal extension of the sponge zones are $(L_{1a}, L_{1b}) = (25.0h_0, 62.5h_0)$. The entire computational domain is discretized using $(n_1, n_3) = (1081, 32)$ grid points. The vertical dimension changes according to the bed slope S, all vertical quantities are shown in Table 2. A time step of $\Delta t = 0.0125$ is employed for a total of 3.2×10^5 iterations, except for cases with $S = 10\%$ that demand more runtime and require a total of 4.8×10^5 iterations.

6.1. Transient state

The complete flow evolution is available as Supplementary Content (see Appendix A), including the spanwise-averaged concentration fields and the depth-averaged concentration fields for all cases. The simulations are arranged vertically according to the bed slope S and horizontally according to the settling velocity u_s. All features of the plunging flow in a tilted bed (see Fig. 1) can be seen, including the three main regions: depth-limited plume, plunging zone and underflow region (both the head and the body of the turbidity current).

Fig. 4 exhibits the spanwise-averaged concentration c for case 5.0–15 ($S = 5\%$ and $u_s = 0.0015$) for dimensionless times 125, 250, 500, 1000 and 2000 from (a) to (e), respectively, where the colored lines indicate the layer-averaged flow height H. Then, the other layer-averaged quantities: (f) Velocity U, (g) concentration C and (h) densimetric Froude number Fr, calculated by (9) and (11). The dashed black lines represent the initial assumptions for obtaining the plunging criterion. According to (12), since the flow rate is constant at the depth-limited zone (and is unitary in dimensionless terms) it can be assumed that the flow velocity is the inverse of the channel's depth $h(x_1) = Sx_1 + 1$. The concentration $C(x_1)$, in turn, decays exponentially with x_1 due to the settling velocity u_s and the shape factor of the concentration profile r_0, assumed as unitary. Finally, the expected variation in the densimetric Froude number $Fr(x_1)$ can be obtained by rearranging Eq. (13). The three quantities are then written as

$$U(x_1) = 1/h(x_1), \tag{15a}$$

$$C(x_1) = \exp(-u_s r_0 x_1), \tag{15b}$$

$$Fr(x_1) = Fr_0 \left(h(x_1) \exp\left[-\xi \frac{h(x_1) - 1}{3} \right] \right)^{-3/2}, \tag{15c}$$

notice they are valid just upstream plunging, at the depth-limited zone. Concerning the time evolution of the spanwise-averaged concentration, we notice that both the plunge zone and the underflow head are visible early on, and both move downstream as time progresses. At $t \approx 2000$, the current head leaves the test section, while the plunge position tends to a stationary position. The coloring gradually becomes lighter with x_1, since the sedimentation reduces the concentration of suspended material. Both current body and head present an intense mixture between the submerged turbidity current and the ambient fluid, mainly due to the Kelvin–Helmholtz vortices and the lobe-and-cleft structures present in these regions. The depth-averaged velocity U in (f) shows good agreement between the measured velocities and (15a) in the depth-limited zone, between the channel entrance and the plunge point. Downstream plunging, the reduction in height and the mixture between the submerged flow and the ambient fluid result in new values for velocity, greater than the previous ones. It is noteworthy that for initial times (125 and 250) the measured velocity is visibly above the others, this is justified by the appearance of a recirculation bubble near the entrance while the recycling technique at the entrance of the domain is not yet fully established. Once the turbulence in the recycling channel is fully developed, there is reattachment of the flow to the bed, and the measured speeds approach the estimated values. The depth-averaged concentration C is displayed in Fig. 4g. We observe exponential decaying as a function of the settling speed, in good agreement with the initial assumption (15b) upstream of the plunge zone. Downstream of plunging, the mixing at the body and head of the submerged flow dilutes the layer-averaged concentration. The curves also work as an indicator for the temporal evolution of the front position x_f, which is obtained for the highest value of x_1 where the concentration is non-zero. The densimetric Froude number Fr is presented in Fig. 4h. It is remarkable how the evolution of Fr with time remains close to the prediction (15c) upstream of plunging, even during the initial flow development. It is observed that once the front of the turbidity current reaches a fully developed state ($t = 1000$), the densimetric Froude number in the region is close to unity, which is consistent with the experimental results of Sequeiros et al. (2009) and Sequeiros et al. (2018). After this, the head leaves the test section and the underflow tends to a quasi-stationary state ($t = 2000$), a Froude number around 2.0 is observed downstream plunging (where $x_1 = 250$). Fr is also used as a marker for obtaining the temporal evolution of the plunge position x_p, since it is observed at Froude's absolute minimum position.

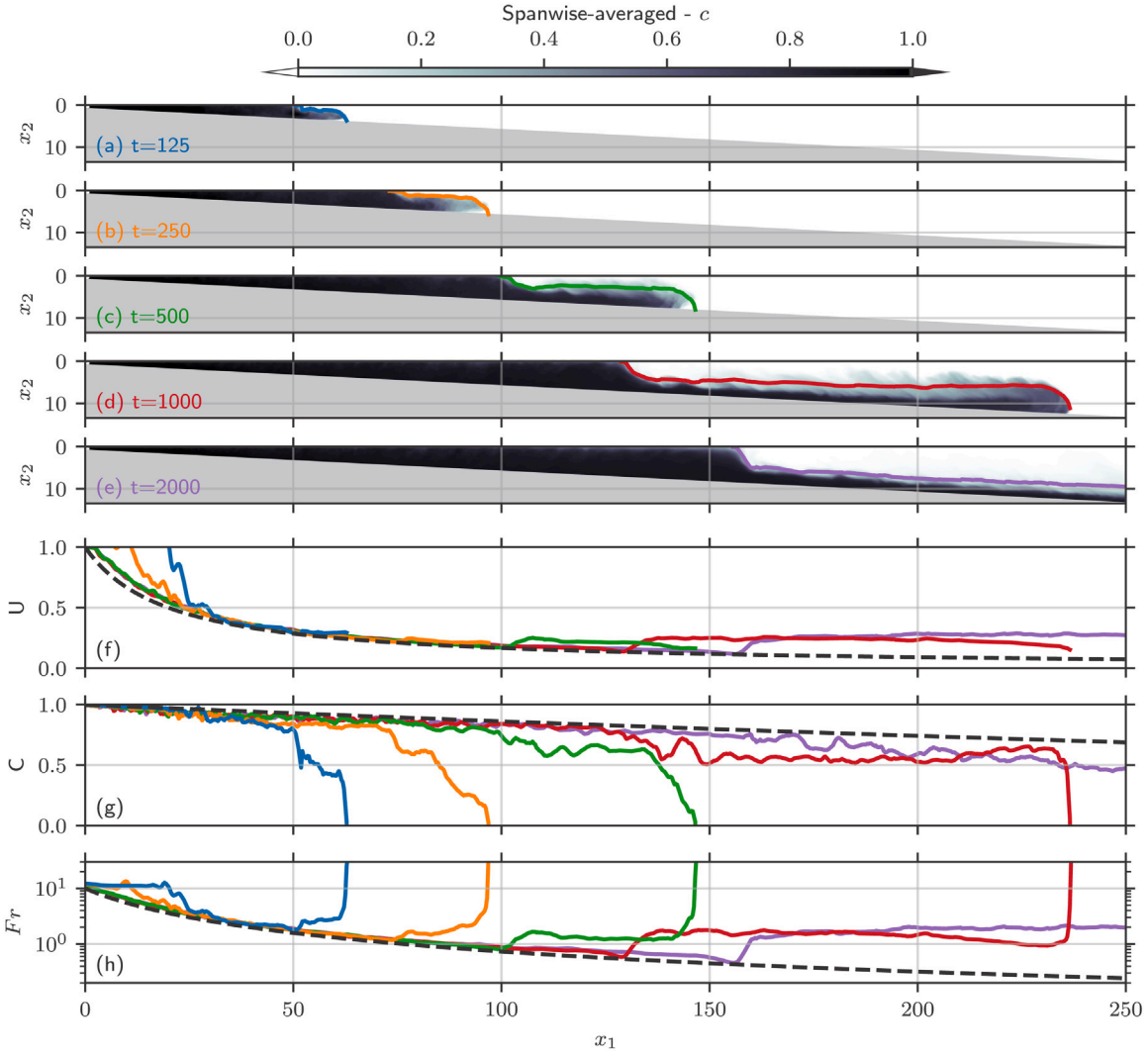

Fig. 4. Spanwise-averaged concentration field c for case 5.0–15 for times 125, 250, 500, 1000 and 2000 from (a) to (e), in addition to layer-averaged flow height H. The other depth-averaged quantities: (f) Velocity U, (g) concentration C and (h) densimetric Froude number Fr. The black dashed lines correspond to Eq. (15). (For interpretation of the references to color in this figure legend, the reader is referred to the web version of this article.)

The spatio-temporal data (x_i and t) are reduced to 2D (x_1 and t) by means of spanwise and layer averages, computed according to (11). Then the variables are used to track in time the two main features of the plunging flow: first, the front position x_f is obtained where the layer-averaged concentration C is equal to zero; second, the plunging position x_p occurs at the minimum value for the densimetric Froude number Fr. The front velocity is defined as $u_f = dx_f/dt$, and a moving average in time is applied in order to reduce the noise in these curves. The corresponding channel depth h_p and densimetric Froude number Fr_p are obtained where $x_1 = x_p$. All curves are presented in Fig. 5. The maximum front velocity u_f occurs right at the beginning of the simulations (Fig. 5b), then the front faces a period of deceleration and reaches a state of constant velocity. Subsequently the front leaves the test section. The relation between settling velocity u_s and initial Froude number Fr_0 provided by (13) produced an interesting effect; the effective Froude numbers at the incipient plunging position (Fig. 5e, for $t < 1000$) are relatively close for a given bed slope S and, as a consequence, the initial development for the plunge point (Fig. 5b) as well as for the front (Fig. 5a) depends only on S for this set of simulations. The cases with $S = 10\%$ demand more run-time in order to get a stable plunge position, as shown in Fig. 5b. Fig. 5c presents the time evolution for the plunging position. Remember that the parameters were computed according to (13), and all simulations are expected to stabilize at $x_p = 150$. In fact, this happened for the five cases. On the other hand, the stable plunge position is downstream of the expected value for the cases with $u_s = 0.0015$ and cases with $S = 10\%$, and the plunging is upstream of the expected value for case $S = 1.25\%; u_s = 0.003$. For the cases with small slope $S = 1.25\%$, this movement of the stable plunging position presents less impact for depth at plunging zone, as shown in Fig. 5c. More vigorous initial mixing is expected in the plunging zone for larger slopes, and as a consequence the Froude number at plunging is low, as shown in the model of Parker and Toniolo (2007). That is why the plunging for cases $S = 10\%$ occurs downstream of our prediction.

6.2. Steady state

In this section, the spatio-temporal data (x_i and t) are reduced to 1D (x_1), so all variables can be analyzed as function of the streamwise direction only. Toward this end, a time average is employed for $2000 \leq t \leq 4000$, except for cases with $S = 10\%$, where the period is $4000 \leq t \leq 6000$. Then, the spanwise and layer averages are computed according to (11). This data is used for the values presented in Table 1, for reference, with respect to measurements at the plunge point and downstream at the underflow. It presents distance for plunging x_p, depth, concentration and densimetric Froude number at the plunge

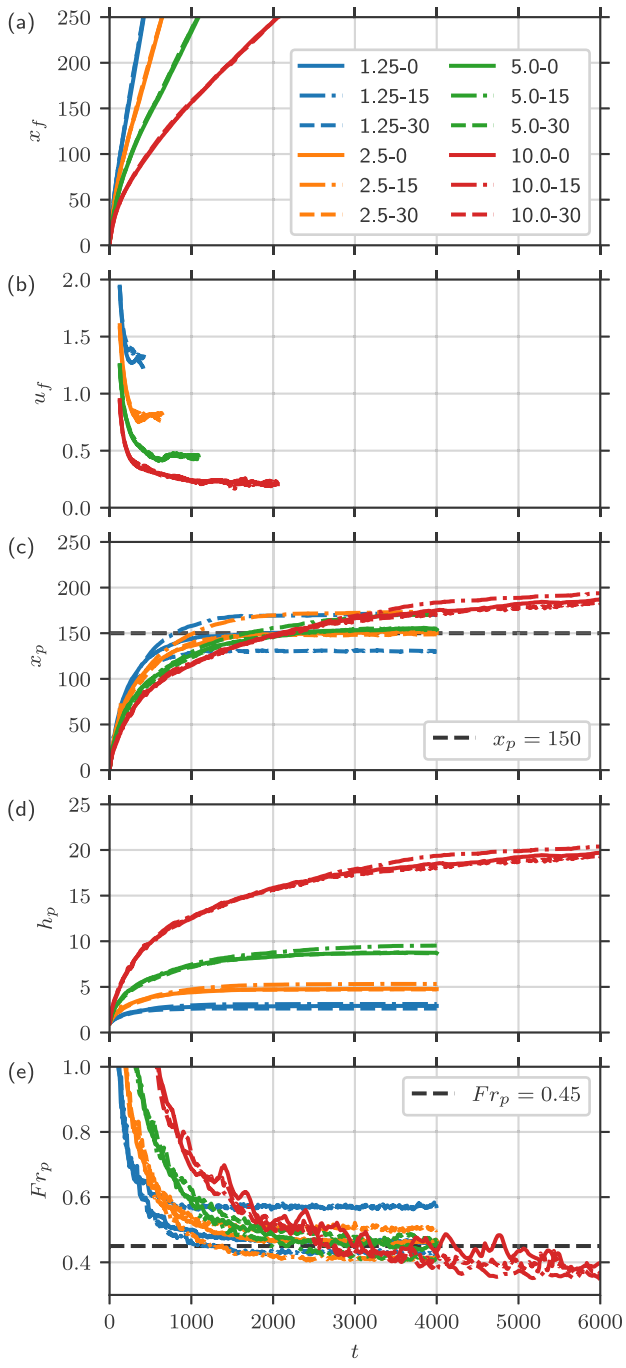

Fig. 5. Time evolution of (a) front position x_f, (b) front velocity u_f, (c) distance for plunge location x_p, (d) channel depth at the plunging position h_p and (e) densimetric Froude number at plunge point Fr_p, $Fr_p = 0.45$ is shown for reference.

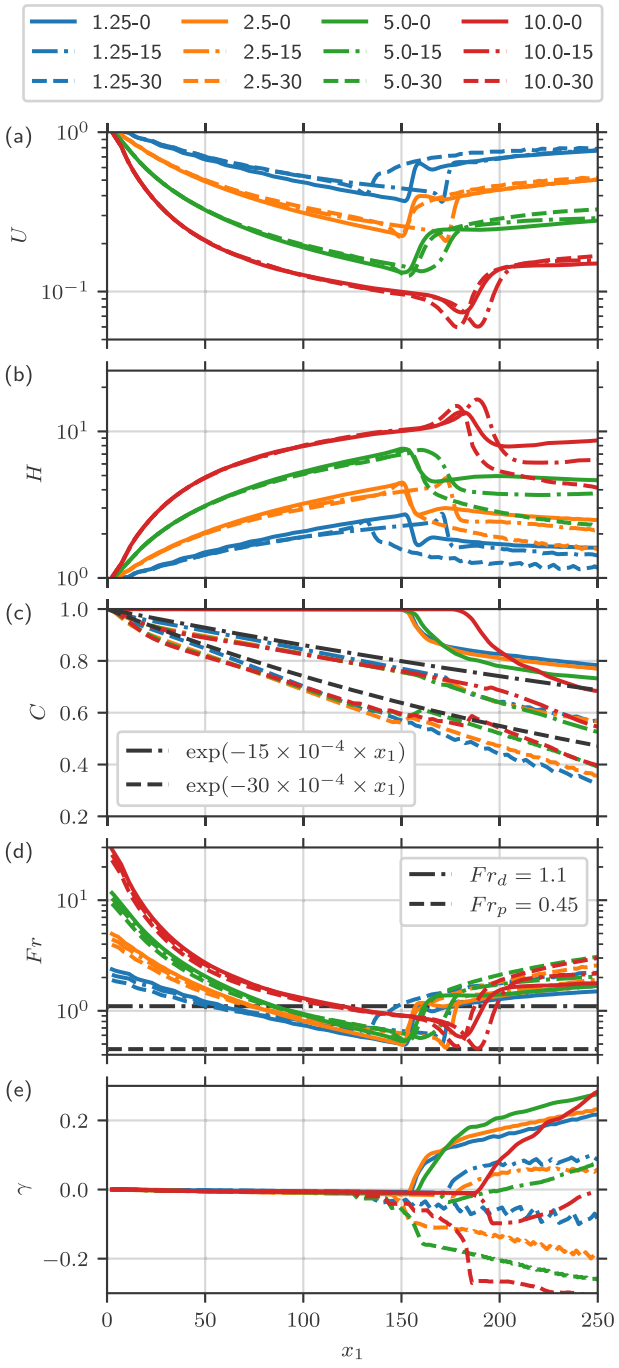

Fig. 6. Steady-state time averaged spatial evolution of layer averaged: (a) velocity U, (b) flow depth H and (c) concentration C, computed according to (11). Besides, the (d) corresponding densimetric Froude number ($Fr_p = 0.45$ and $Fr_d = 1.1$ are shown for reference), computed according to Eq. (9), and (e) mixing coefficient γ.

point (H_p, C_p and Fr_p, respectively) and downstream, at the end of the test section (H_d, C_d and Fr_d, respectively), besides the mixing coefficient $\gamma_d = Q_d/Q_0 - 1$. The complete spatial variation of the variables in the steady-state can be observed in Fig. 6.

The flow rate is constant in the depth-limited plume (see Fig. 1). Therefore, the velocity U (Fig. 6a) in this zone decays with x_1, while the flow depth H (Fig. 6b) increases and the mixing coefficient γ (Fig. 6e) is zero upstream of the plunge point. The concentration C (Fig. 6c) decays due the settling of the suspended material (when $u_s \neq 0$), which reduces the effective concentration at the plunge point. The densimetric Froude number (Fig. 6d), computed according to (9), has a maximum at the beginning of the channel, due to the tilted bed, the flow depth increasing with x_1 reduces the local Froude number, on the other hand, the sedimentation decreases the depth-averaged concentration with x_1, increasing the local Froude number. In the plunge zone, the flow reaches its maximum depth H, besides minimum values for velocity U and densimetric Froude number Fr. At this point, the reduction in flow depth and the conversion from vertical to streamwise velocity produce an acceleration over a very short distance (Fig. 6 a and b). In the underflow density current, the velocity U and depth H are almost constant, while the concentration keeps decaying due to the

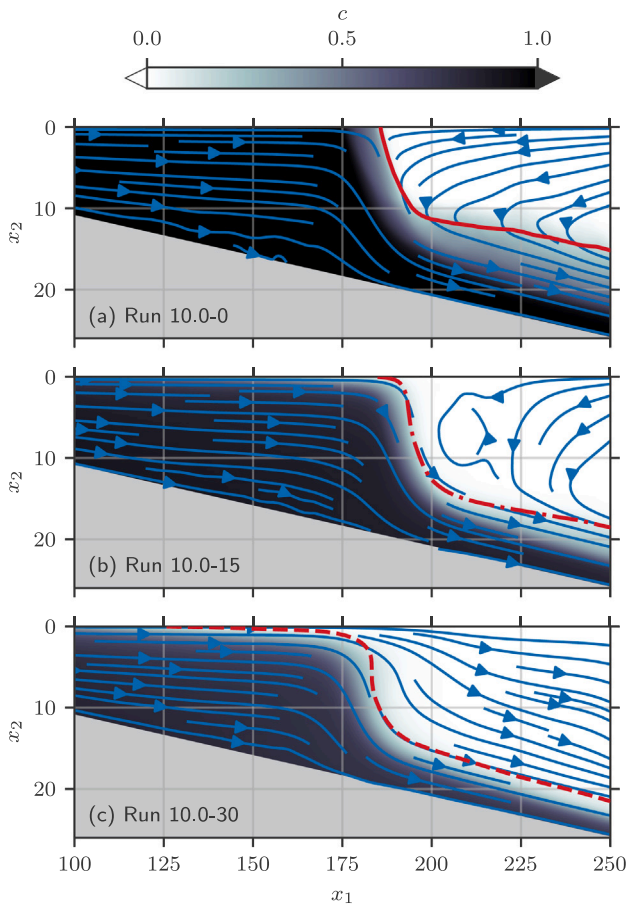

Fig. 7. Time and spanwise averaged concentration and velocity field, represented by color scheme and arrows, respectively. Red lines indicate the interface between the ambient fluid and the underflow density current, considered in this work where $u_1 c = 0.025$. (For interpretation of the references to color in this figure legend, the reader is referred to the web version of this article.)

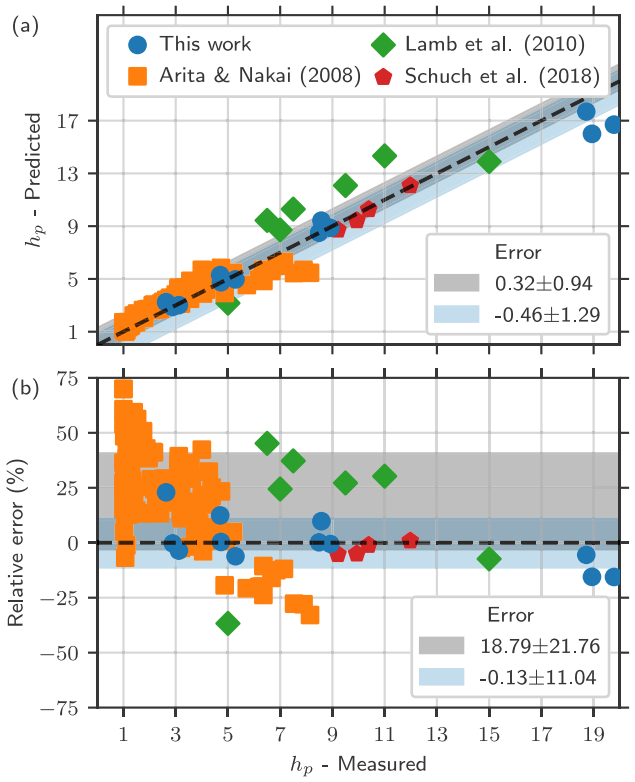

Fig. 8. (a) Flow depth at plunge point versus flow depth at plunge point predicted by Eq. (13). (b) Same results, in terms of the relative error. In both figures, the dashed line indicates the 1:1 correlation, gray and blue region indicates the area covered by the standard deviation for the error of the entire data and only the cases from this work, respectively. (For interpretation of the references to color in this figure legend, the reader is referred to the web version of this article.)

mixing with the ambient fluid and settling, once the numerical model does not allow entrainment from bed sediment. The densimetric Froude number in the plunge zone increases from $Fr_p \approx 0.45$ to $Fr_d \approx 1.1$ just downstream, which is in agreement with previous studies in the same configuration (Schuch et al., 2018; Lamb et al., 2010), and it keeps increasing further downstream, in the developed underflow zone. All simulated cases are supercritical (e.g., $Fr_d > 1$), which is expected when the bed slope is steeper than 1%, notice the value for Fr_d depends mostly on the bed slope, and secondary on bed roughness and settling velocity, as explained in Sequeiros (2012).

The mixing between the ambient fluid and the underflow density current starts downstream of plunging, as shown in Fig. 6e. For most cases, a positive value indicates that the flow rate continuously grows due to the incorporation of the ambient fluid into the underflow. However, the opposite is observed for the cases with high settling velocity $u_s = 0.003$, the negative value for the mixing coefficient indicates that the underflow is losing fluid to the ambient. As a consequence, the ambient flow, which usually points in the opposite direction of the current, is flowing in the same direction as the underflow for those cases. This phenomenon, exemplified in Fig. 7 for the cases with $S = 10\%$, is explained by the thin fresh-water layer formed near the top due to the settling of suspended material, in both depth-limited and underflow zones. The density in this layer is lower than the current, so the underflow loses its volume to the ambient, in a detrainment process. The difference at the interface between the ambient and the underflow in the plunge zone is also noticeable. It is observed as a sharp edge when $u_s = 0$ (Fig. 7a), on the other hand, a smooth transition is observed when the settling speed increases (Fig. 7 b and c). Notice that the plunge position x_p is nearly the same for the three cases, even considering the opposite dynamics in the ambient flow.

6.3. Plunging criteria

In this section, the depths at the plunge points measured from the twelve numerical simulations are compared with the predicted values computed from Eq. (13), proposed in this work. Note that the depth at plunge point $h_p = x_p S + 1$ is not necessarily the same value obtained for the layer-averaged depth H_p (11b), nevertheless, just data for the first is available in the literature and so it is used in this section for comparison. The results are presented in Fig. 8 with the experimental data of Arita and Nakai (2008) and Lamb et al. (2010), besides the earlier numerical work of Schuch et al. (2018), considering $Fr_p = 0.45$ and $r_0 = 1.5$ as initial estimates, both values reported by Lamb et al. (2010) for a similar set-up. The results in Fig. 8a show good agreement between the values, for an absolute averaged difference of 0.32 ± 0.94 for the entire data (gray region) and -0.46 ± 1.29 only for the cases of this study (blue region). The relative error is more relevant in this comparison, the results presented in Fig. 8b show some scattering for the experimental data, for a relative error of 18.79 ± 21.76. This can be explained by a series of effects that are not taken into account by the presented numerical framework, for instance, the free surface at the top boundary, variations at the bed position, bed friction due to bedforms, and others. On the other hand, since the proposed equation does not take these effects into account either, the relative error is reduced to -0.13 ± 11.04 if just the twelve cases of this study are considered.

An improvement to the prediction would be possible with regard to the initial estimates for the values of the densimetric Froude number at the plunge point Fr_p and the shape factor for the concentration vertical profile r_0. The results presented at Table 1 indicate $Fr_p = 0.51 \pm 0.047$ and $r_0 = 1.22 \pm 0.073$, computed from Eq. (12b). There is no reason to define these parameters as constant, since their values may be a function of some of the flow aspects, for instance, the bed slope angle, the mixing rate, and the total friction coefficient. However, there is no visual correlation between the values of Fr_p, r_0 and the different parameters considered in this study (initial densimetric Froude number Fr_0, bed slope S and particle settling velocity u_s).

7. Conclusions

A new equation for the plunging criterion was developed; it differs from previous studies by including the role that the settling velocity and the bed slope (or the ratio between both) have on the necessary depth for plunging. The study establishes a parallel between the initial densimetric Froude densimetric Fr_0 and its correspondent value at the plunge point Fr_p, by means of three assumptions that describe the streamwise variation for the volumetric flow discharge, concentration and flow height. The proposed equation has no analytical solution, however, it can be solved numerically as a function of three characteristic flow parameters: settling velocity u_s, bed slope S and the initial densimetric Froude number Fr_0. In addition, there are two constants that need to be estimated: densimetric Froude number at the plunge point Fr_p and the shape factor of the vertical concentration profile r_0. Here, the turbulence-resolving three-dimensional simulations performed a fundamental role, since they provide information on the flow for any position in time and space, by allowing to verify the initial hypotheses established for the proposed plunging criterion. For this purpose, twelve numerical simulations were designed, combining four values for bed slope and three different settling velocities, in addition to the experimental data available in the literature, and good agreement was found between them. Once the validation of the initial premises for the streamwise variation of the main flow quantities was successful, it is highlighted that they can be applied as models for future studies. A negative mixing coefficient was observed for the first time for the hyperpycnal flow in a tilted channel. This indicates that if the settling velocity of the suspended material is high enough, the submerged flow may lose fluid to the environment (detrainment), instead of incorporating fluid. Once this occurs, the ambient flows in the same direction as the submerged flow, and the plunge point is no longer a stagnation point (see Fig. 7c), as reported by several other studies. The proposed plunging criterion may assist in the design of future experimental or numerical works, mainly in the context of Direct Numerical Simulation (DNS), which have a high computational cost. DNS may be a future step for the study of the plunging flow tilted channel, once the computational resources are available to do so.

Computer code availability

This work is based on the open-source Navier–Stokes solver Xcompact3d. The code is available since 2006, written in Fortran-90, OS independent (Fortran-90 and MPI compilers are required), licensed under the GNU General Public License v3.0, more information can be found at its repository github.com/xcompact3d/Incompact3d. A forked version from the original code was developed for this work in order to simulate the plunging flow, it is available at github.com/fschuch/incompact3d_plunging_criterion.

CRediT authorship contribution statement

Felipe N. Schuch: Conceptualization, Data curation, Formal analysis, Investigation, Methodology, Software, Validation, Visualization, Writing - original draft. **Eckart Meiburg:** Conceptualization, Supervision, Resources, Writing - review & editing. **Jorge H. Silvestrini:** Project administration, Conceptualization, Supervision, Resources, Writing - review & editing.

Declaration of competing interest

The authors declare that they have no known competing financial interests or personal relationships that could have appeared to influence the work reported in this paper.

Data availability

Data included in the analysis for this work is available on the Zenodo data repository https://doi.org/10.5281/zenodo.4044388.

Acknowledgments

This study was supported by Petrobras S.A. and financed in part by the Coordenação de Aperfeiçoamento de Pessoal de Nivel Superior - Brasil (CAPES) - Finance Codes 88887.154060/2017-00 and 88881.187490/2018-01. The authors acknowledge the High–Performance Computing Laboratory of the Pontifical Catholic University of Rio Grande do Sul (LAD-IDEIA/PUCRS, Brazil) for providing support and technological resources, which have contributed to the development of this project and to the results reported within this research.

Appendix A. Supplementary data

Supplementary material related to this article can be found online at https://doi.org/10.1016/j.cageo.2021.104880.

References

Akiyama, J., Stefan, H.G., 1984. Plunging flow into a reservoir: Theory. J. Hydraul. Eng. 110, 484–499.
Arita, M., Nakai, M., 2008. Plunging conditions of two-dimensional negative buoyant surface jets released on a sloping bottom. J. Hydraul. Res. 46, 301–306.
Bartholomew, P., Deskos, G., Frantz, R.A., Schuch, F.N., Lamballais, E., Laizet, S., 2020. Xcompact3D: An open-source framework for solving turbulence problems on a cartesian mesh. SoftwareX 12, 100550.
Chamoun, S., De Cesare, G., Schleiss, A.J., 2016. Managing reservoir sedimentation by venting turbidity currents: A review. Int. J. Sediment Res. 31, 195–204.
Dai, A., Cantero, M.I., García, M.H., 2007. Plunging of two-dimensional gravity currents. In: Proc., 5th Int. Symp. on Environmental Hydraulics, IAHR, Temp, Ariz.
Dai, A., García, M.H., 2009. Discussion of "Note on the analysis of plunging of density flows" by Gary Parker and Horacio Toniolo. J. Hydraul. Eng. 135, 532–533.
Dairay, T., Lamballais, E., Laizet, S., Vassilicos, J.C., 2017. Numerical dissipation vs. subgrid-scale modelling for large eddy simulation. J. Comput. Phys. 337, 252–274.
Ellison, T., Turner, J., 1959. Turbulent entrainment in stratified flows. J. Fluid Mech. 6, 423–448.
Farrell, G., Stefan, H., 1986. Buoyancy Induced Plunging Flow into Reservoirs and Coastal Regions. Project Report, No. 241, St, Anthony Falls Hydr. Lab., University of Minnesota.
Garcia, M.H., 1994. Depositional turbidity currents laden with poorly sorted sediment. J. Hydraul. Eng. 120, 1240–1263.
Gautier, R., Laizet, S., Lamballais, E., 2014. A DNS study of jet control with microjets using an immersed boundary method. Int. J. Comput. Fluid Dyn. 28, 393–410.
Grinstein, F.F., Margolin, L.G., Rider, W.J., 2007. Implicit Large Eddy Simulation: Computing Turbulent Fluid Dynamics. Cambridge university press.
Henniger, R., Kleiser, L., Meiburg, E., 2010. Direct numerical simulations of particle transport in a model estuary. J. Turbul. N39.
Horner-Devine, A.R., Hetland, R.D., MacDonald, D.G., 2015. Mixing and transport in coastal river plumes. Annu. Rev. Fluid Mech. 569–594.
Julien, P.Y., 2010. Erosion and Sedimentation. Cambridge University Press.
Kassem, A., Imran, J., 2001. Simulation of turbid underflows generated by the plunging of a river. Geology 29, 655–658.
Laizet, S., Lamballais, E., 2009. High-order compact schemes for incompressible flows: A simple and efficient method with quasi-spectral accuracy. J. Comput. Phys. 228, 5989–6015.
Laizet, S., Li, N., 2011. Incompact3d: A powerful tool to tackle turbulence problems with up to $O(10^5)$ computational cores. Internat. J. Numer. Methods Fluids 67, 1735–1757.
Lamb, M.P., McElroy, B., Kopriva, B., Shaw, J., Mohrig, D., 2010. Linking river-flood dynamics to hyperpycnal-plume deposits: Experiments, theory, and geological implications. Bulletin 122, 1389–1400.
Lamb, M.P., Mohrig, D., 2009. Do hyperpycnal-flow deposits record river-flood dynamics? Geology 37, 1067–1070.

Lamballais, E., Fortuné, V., Laizet, S., 2011. Straightforward high-order numerical dissipation via the viscous term for direct and large eddy simulation. J. Comput. Phys. 230, 3270–3275.
Lee, H.-Y., Yu, W.-S., 1997. Experimental study of reservoir turbidity current. J. Hydraul. Eng. 123, 520–528.
Lele, S.K., 1992. Compact finite difference schemes with spectral-like resolution. J. Comput. Phys. 103, 16–42.
Meiburg, E., Kneller, B., 2010. Turbidity currents and their deposits. Annu. Rev. Fluid Mech. 42, 135–156.
Meiburg, E., Radhakrishnan, S., Nasr-Azadani, M., 2015. Modeling gravity and turbidity currents: Computational approaches and challenges. Appl. Mech. Rev. 67, 40802.
Mulder, T., Syvitski, J.P.M., Migeon, S., Faugeres, J.-C., Savoye, B., 2003. Marine hyperpycnal flows: initiation, behavior and related deposits. A review. Mar. Pet. Geol. 20, 861–882.
Mulder, T., Syvitski, J.P., Skene, K.I., 1998. Modeling of erosion and deposition by turbidity currents generated at river mouths. J. Sediment. Res. 68, 124–137.
Nasr-Azadani, M., Hall, B., Meiburg, E., 2013. Polydisperse turbidity currents propagating over complex topography: comparison of experimental and depth-resolved simulation results. Comput. Geosci. 53, 141–153.
Necker, F., Härtel, C., Kleiser, L., Meiburg, E., 2002. High-resolution simulations of particle-driven gravity currents. Int. J. Multiph. Flow. 28, 279–300.
Parker, G., Garcia, M., Fukushima, Y., Yu, W., 1987. Experiments on turbidity currents over an erodible bed. J. Hydraul. Res. 25, 123–147.
Parker, G., Toniolo, H., 2007. Note on the analysis of plunging of density flows. J. Hydraul. Eng. 133, 690–694.
Porcile, G., Pittaluga, M.B., Frascati, A., Sequeiros, O.E., 2020. Typhoon-induced megarips as triggers of turbidity currents offshore tropical river deltas. Commun. Earth Environ. 1, 1–13.
Sagaut, P., 2006. Large Eddy Simulation for Incompressible Flows: An Introduction. Springer Science & Business Media.
Schuch, F.N., Pinto, L.C., Silvestrini, J.H., Laizet, S., 2018. Three-dimensional turbulence-resolving simulations of the plunge phenomenon in a tilted channel. J. Geophys. Res. Oceans 123, 1–13.
Schuch, F.N., Silvestrini, J.H., Meiburg, E., Laizet, S., 2020. The plunging of hyperpycnal plumes on tilted bed by three-dimensional large-eddy simulations. In: 12th Spring School on Transition and Turbulence. ABCM, Blumenau, SC, Brazil, http://dx.doi.org/10.5281/zenodo.3968993.
Sequeiros, O.E., 2012. Estimating turbidity current conditions from channel morphology: A froude number approach. J. Geophys. Res. Oceans 117.
Sequeiros, O.E., Mosquera, R., Pedocchi, F., 2018. Internal structure of a self-accelerating turbidity current. J. Geophys. Res. Oceans 123, 6260–6276.
Sequeiros, O.E., Naruse, H., Endo, N., Garcia, M.H., Parker, G., 2009. Experimental study on self-accelerating turbidity currents. J. Geophys. Res. Oceans 114, 1–26.
Sequeiros, O.E., Pittaluga, M.B., Frascati, A., Pirmez, C., Masson, D.G., Weaver, P., Crosby, A.R., Lazzaro, G., Botter, G., Rimmer, J.G., 2019. How typhoons trigger turbidity currents in submarine canyons. Sci. Rep. 9, 1–15.
Singh, B., Shah, C., 1971. Plunging phenomenon of density currents in reservoirs. Houille Blanche 59–64.